J Adv Ceram

Research Article

High-throughput screening of $Ta_{1-x}Hf_xC_y$ ceramics for mechanical and oxidation performance optimization for ultra-high-temperature applications

Xirui Lv[1], Yiming Lei[1], Jinyu Shi[1,2], Jie Zhang[1,✉], Jingyang Wang[1]

Cite this article: Lv X, Lei Y, Shi J, et al. *J Adv Ceram* 2026, **15**(3): 9221252. https://doi.org/10.26599/JAC.2026.9221252

ABSTRACT: $Ta_{1-x}Hf_xC_y$ ternary ceramics are highly valued in hypersonic vehicles, and a precise composition design is promising to simultaneously reduce their intrinsic brittleness and enhance their protective capability during oxidation. Herein, the composition-dependent mechanical properties and oxidation behaviors of $Ta_{1-x}Hf_xC_y$ ternary ceramics over a broad composition range (x = 0.22 to 0.78, y = 0.66 to 1.00) are efficiently investigated through combinatorial and high-throughput (CHT) experimentation to pave the way for targeted development of novel carbide candidates. Evolution trends in hardness and modulus reveal that the composition range with x = 0.22 to 0.60 and y = 0.80 to 1.00 is promising to reach an optimal balance between hardness and toughness, which results from competing effects between solid solution strengthening and bonding characteristic transition. High-throughput oxidation elucidates the phase constitution and compactness of oxidation products with various Ta/Hf distributions and temperatures. The accurate compositional range for the formation of a single-phase dense Hf–Ta–O compound layer shifts to a Ta-rich region (x = 0.50 to 0.60) due to the preferential formation of Ta-doped HfO_2 and the structural characteristics of Hf–Ta–O compounds that accommodate compositional deviations. Regarding the broad compositional space of $Ta_{1-x}Hf_xC_y$, the effects of composition on both mechanical properties and oxidation behavior are systematically investigated, providing fundamental design guidelines and an optimal composition range that holds significant promise for application in subsequent research.

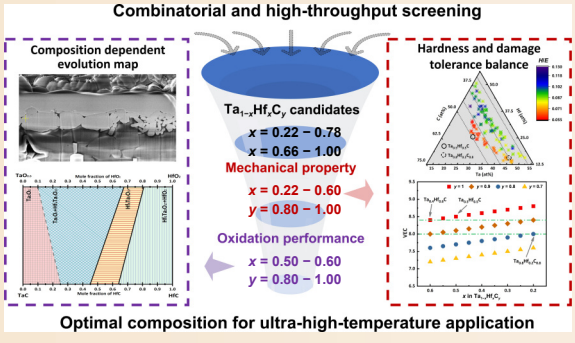

KEYWORDS: $Ta_{1-x}Hf_xC_y$ ternary ceramics; combinatorial material chips; high-throughput screening; mechanical properties; oxidation resistance

1 Introduction

$Ta_{1-x}Hf_xC$ ternary carbides have attracted considerable attention as structural materials and protective coatings in thermal protection systems (TPS), which are applied as sharp leading edges, nose caps, and flight control components of aerospace vehicles exposed to temperatures exceeding 2000 °C in dissociated air during hypersonic flight [1]. Among all ultrahigh temperature ceramics (UHTCs), $Ta_{1-x}Hf_xC$ ternary carbides exhibit a uniquely high melting point, and $Ta_{0.8}Hf_{0.2}C$ has been regarded as the most refractory material with a melting point of 4300 K [2]. In addition, the strong chemical bonding between transition metal atoms (Ta,Hf) and C significantly improves their hardness and modulus. Notably, $Ta_{0.5}Hf_{0.5}C$ exhibits a local maximum hardness (36 GPa) and modulus (559 GPa) within this system in the nanoindentation test [3]. Moreover, previous ablation investigations have demonstrated that the formation of complex Hf–Ta–O compounds enables the structural densification of the oxidation scale and reduces the ablation rate [4]. However, the intrinsic brittleness of these carbides has hindered their performance, and their oxidation or ablation resistance still needs to be optimized to meet the demands of extreme aerospace applications [5].

During ultrahigh-temperature application, the brittleness of $Ta_{1-x}Hf_xC$ ceramics leads to weak thermal shock resistance, making them highly susceptible to micro cracking or peeling during abrupt temperature changes and mechanical erosion [6]. It is well accepted that the integration of bonding characteristics and solid solution strengthening in $Ta_{1-x}Hf_xC$ contributes to their outstanding hardness and modulus, while these features also result in inevitable brittleness. Continuous efforts have been devoted to promoting the toughness of $Ta_{1-x}Hf_xC$ ternary carbides. The most common approach is to induce a secondary phase in the form of

[1] Advanced Ceramics and Composites Division, Shenyang National Laboratory for Materials Science, Institute of Metal Research, Chinese Academy of Sciences, Shenyang 110016, China. [2] School of Materials Science and Engineering, University of Science and Technology of China, Shenyang 110016, China.

✉ Corresponding author. E-mail: jiezhang@imr.ac.cn

Received: November 3, 2025; Revised: December 24, 2025; Accepted: January 14, 2026

particles to generate an effective toughening mechanism in $Ta_{1-x}Hf_xC$ bulks. Zhang *et al.* [7] promoted the fracture toughness (K_{IC}) of $Ta_{0.8}Hf_{0.2}C$ bulk samples from 3.7 to 5.4 MPa·m$^{1/2}$ through doping platelet-like SiC, which promoted crack branching and bridging behaviors. The K_{IC} was promoted from 2.9 for $Ta_{0.5}Hf_{0.5}C$ to 6.5 MPa·m$^{1/2}$ by crack deflection at the carbide/HfO_2 interface in $Ta_{0.5}Hf_{0.5}C$–5 vol% HfO_2 composites [8]. In addition, one-dimensional reinforcements, such as HfC nanowires [9] and $Ta_{1-x}Hf_xC$ nanowires [10], have been directly incorporated into $Ta_{1-x}Hf_xC$ coatings to hinder crack propagation and reduce the ablation rates. Recently, a more straightforward approach has been highlighted: The mechanical properties of transition metal carbides, including strength and plasticity, can be balanced through precise chemical composition design. Smith *et al.* [11] reported that the deformation slip behavior of $Ta_{1-x}Hf_xC$ ceramics was promoted with properly increasing Ta content, and a series of dislocations initiated by indentation demonstrated the promoted plasticity of Ta-rich samples. Manipulating carbon deficiency has been proposed as an additional strategy. For instance, $Ta_{0.8}Hf_{0.2}C_{0.8}$ was experimentally verified to possess both plasticity (Pugh's ratio k = 0.41) and ultrahigh nanohardness (41.3 GPa) [12]. This approach aims to achieve an optimal balance between two competing effects: solid solution strengthening, driven by cation sublattice diversity, and chemical bond weakening, caused by a reduction in carbon content [13]. Therefore, extensive experimental and computational studies are required to identify the optimal chemical composition that balances these trade-off mechanisms.

More critically, the composition design strategy that simultaneously regulates cation and anion species in the sublattice has also drawn considerable attention in promoting the oxidation resistance of transition metal carbides [14]. For instance, a proper carbon vacancy will facilitate the formation of carbonaceous oxides, which serve as a dense oxygen barrier to enhance the initial oxidation resistance [15]. Thereafter, a precise design in the stoichiometric ratio of transition metallic elements will accurately promote the formation of oxidation products with high melting points [16], high phase stability [17], and low oxygen penetration rates [18], contributing to a lower oxidation rate, thinner oxidation scale thickness, and reduced mass change rate. Previous studies have demonstrated that for Ta–Hf–C ceramics, Ta-rich compositions generate too many low-melting-point Ta oxides, which is detrimental for ablation resistance, and the formation of complex Ta–Hf–O oxides promotes the stability and completeness of the ablation layer, which are benchmarks for superior ablation resistance [4,19]. Thus, the main efforts in the compositional design of Ta–Hf–C ceramics are devoted to obtaining a greater fraction of complex Hf–Ta–O compounds that generate densely packed, adherent, and thermal-shock resistant oxide scales with low oxygen conductivity. A HfO_2–Ta_2O_5-temperature phase diagram has been established experimentally, in which single-phase $Hf_6Ta_2O_{17}$ is obtained in the compositional range from 20 mol% Ta_2O_5–80 mol% HfO_2 (Hf/Ta = 2) to 11.2 mol% Ta_2O_5–88.8 mol% HfO_2 (Hf/Ta = 4) [20]. Moreover, thermodynamic modeling of the Hf–Ta–O compounds reveals that their structures are metastable when the Ta/Hf ratio ranges from 2 to 3, indicating that the optimal composition range is between 3HfC–1TaC and 4HfC–1TaC [21]. During a practical oxidation or ablation process, different metallic components oxidize sequentially due to thermodynamic mechanisms, and then the competitive formation between simple oxides (such as HfO_2 or Ta_2O_5) and complex compound oxides (such as $Hf_6Ta_2O_{17}$) contributes to the final oxide scale. This complexity demonstrates that designing the Ta/Hf ratio solely based on the reaction behavior or stability of individual oxides is insufficient. Furthermore, the current understanding remains inadequate to explain the oxidation behaviors of multicomponent carbides. For instance, studies based on direct oxidation tests of $Ta_{1-x}Hf_xC$ ceramics usually conclude that $Ta_{0.5}Hf_{0.5}C$ exhibits the highest oxidation resistance among tested $Ta_{1-x}Hf_xC$ compositions (x = 0.2, 0.5, 0.75, and 0.8) [22]. The knowledge gap stems from the lack of fundamental thermodynamic data for complex/ordered compounds, which limits the quantitative analysis of preferential oxidation as a function of composition in multiprincipal materials [23,24]. Moreover, owing to the inherent challenges in sintering, processing, and characterization of these UHTCs, conventional experimentation usually focuses on discrete single-composition specimens, such as equimolar binary to quaternary transition metallic carbides, which hinders establishing a systematic understanding of the oxidation thermodynamics across compositions. Notably, $Ta_{1-x}Hf_xC$, which combines typical group IVB (Hf) and VB (Ta) transition metals, forms a complete solid solution across the whole compositional range, making it an ideal model system for probing composition-dependent oxidation behavior and thermodynamics. To address these challenges, a transformative research paradigm is needed to investigate oxidation behavior in near-continuously graded $Ta_{1-x}Hf_xC$ ceramics, which will enable correlation between composition-dependent experimental oxidation behavior and thermodynamic mechanisms and ultimately guide judicious compositional design for multicomponent carbides.

Recently, combinatorial and high-throughput (CHT) experimentation has emerged as a promising methodology to more efficiently discover and optimize materials, as it covers the entire compositional range instead of being restricted to several discrete points. Leveraging compositional gradients and CHT characterization, a large material property database is generated by analyzing hundreds of samples in a single experiment. The obtained database has been used to elucidate trends and mechanisms of a series of material characteristics, including phase constitution, crystal structure, mechanical properties, and corrosion resistance [25]. In CHT investigations, combinatorial material chips obtained by physical vapor deposition techniques have been proven to be a powerful tool for rapid material studies in constructing phase diagrams, establishing composition–property relationships, optimizing chemical compositions, and discovering new materials [26]. CHT oxidation tests have demonstrated well-established feasibility by effectively screening and characterizing oxidation behaviors across diverse compositions under varied temperatures (> 1000 °C) and atmospheric conditions through a suite of characterization techniques [25]. Faced with UHTCs targeting service temperatures over 1600 °C (even 2000 °C) [27], the design of high-throughput ablation test systems under near-service conditions remains challenging. Given this challenge, the focus for composition design shifts to the key determining properties of the surface oxides. Considering that the phase constitution, melting point, and stability of the surface oxides play a decisive role in oxidation/ablation resistance, it is a well-established research paradigm to design and optimize UHTC compositions primarily through static oxidation experiments, since the oxide products usually form at a relatively lower temperature range [17]. Although temperature can influence the activation energy for the oxidation of individual elements, the inherent thermodynamic order of oxidation among different elements usually remains unchanged and contributes to the coating's behavior during

ablation, critically influencing processes such as liquid-phase formation or volatilization. This fundamental thermodynamic sequence ultimately governs the significance of static oxidation experiments for predicting performance in ultrahigh-temperature service environments [28,29].

In the present work, combinatorial magnetron sputtering deposition was used to prepare $Ta_{1-x}Hf_xC_y$ combinatorial material chips for high-throughput exploration of composition-dependent mechanical properties and oxidation behaviors. The deposition parameters were precisely controlled to generate continuous and broad compositional gradients. Evolution trends of hardness and modulus as a function of Ta/Hf distribution and C content were efficiently obtained through nanoindentation tests to identify the primary candidate compositional range for optimal mechanical behavior. Additionally, the Ta/Hf ratio was optimized based on the composition–temperature–oxidation behavior relationships, including phase constitution, compactness, and oxidation scale stability. This was achieved through parallel high-throughput oxidation investigations, which provided a comprehensive understanding of the oxidation mechanisms from the compositional perspective. Based on these findings, optimal oxidation-resistant $Ta_{1-x}Hf_xC_y$ carbides are recommended for ultrahigh-temperature thermal protection applications.

2 Experimental

2.1 Preparation of $Ta_{1-x}Hf_xC_y$ combinatorial material chip

$Ta_{1-x}Hf_xC_y$ combinatorial material chips were synthesized via a combinatorial magnetron sputtering deposition system (Shenyang Kecheng Vacuum Tech Co., Ltd., China) equipped with Ta, Hf, and C elemental targets (Shanghai Daheng Optics and Fine Mechanics Co., Ltd., China) as well as a stationary substrate holder. The details of the cosputtering preparation system were described in our previous work [26]. Commercial sapphire (single crystal Al_2O_3, polished to root mean square roughness (R_{ms}) < 0.5 nm) and polycrystalline Al_2O_3 (roughly ground to R_{ms} < 500 nm) (Shanghai Daheng Optics and Fine Mechanics Co., Ltd., China) with a diameter of 50 mm were used as substrates. A sapphire substrate with lower roughness was used for the nanoindentation test, and the isotropic thermal expansion coefficient of polycrystalline Al_2O_3 was beneficial for mitigating thermal stresses during oxidation experiments, thereby preventing premature cracking or delamination of thin-film sample patches. Compositional gradients dependent on location were obtained due to deposition on a stationary substrate, and the desired compositional range was achieved by adjusting the sputtering power for each elemental target. Ta, Hf, and C were sputtered at 50–70, 30–80, and 50–150 W, respectively, and $Ta_{1-x}Hf_xC_y$ samples were grown at 550 °C for 2 h with an Ar pressure of 0.4 Pa. A comprehensive description of sputtering target placement is shown in Fig. S1 in the Electronic Supplementary Material (ESM) and sputtering parameter combination is shown in Table S1 in the ESM. Moreover, the as-deposited $Ta_{1-x}Hf_xC_y$ film was divided by a mask, resulting in hundreds of individual thin-film sample patches with a diameter of 3 mm for high-throughput screening.

2.2 Characterization of $Ta_{1-x}Hf_xC_y$ combinatorial material chip

The thickness of the as-prepared sample patches was obtained through a step-profiler (P7, KLA-Tencor, USA). The load force of the stylus was 1 μg, and the scanning speed was 0.1 mm/s. The scanning length was 4 mm to cover the whole sample patch, and the thickness was calculated according to the step height between each sample patch and substrate on the scanning profile. The surface roughness of the as-deposited film sample patches on the sapphire substrate was measured using a laser scanning confocal microscope (Olympus OLS4000, Olympus, Japan). For each sample patch, a central area of 250 μm × 250 μm was scanned with a 50× objective. The acquired 3D topography data were processed with a Gaussian filter using a cutoff wavelength (λ_c) of 80 μm to separate roughness from waviness, and the arithmetic mean roughness (R_a) was determined. The surface morphology of the as-deposited sample patches on the sapphire substrate was obtained through a scanning electron microscope (SEM; GEMINISEM 300, ZEISS, Germany). It should be noted that the characterization of thickness, roughness, and morphology was conducted on a subset of sample patches (approximately 20% of the total) on one combinatorial material chip. These selected points covered key locations, including the center of the substrate (farthest from the targets), the mid-radius position, and the edge (closest to the targets). This selection is representative of the variations in deposition processes, such as deposition efficiency and grain growth orientation, caused by changes in the relative position and angle between the sample patches and the targets. The elemental distribution of combinatorial material chips was analyzed by electron probe microanalyzer (EPMA; 1720H, Shimadzu, Japan) using a focused electron beam with a diameter of 1 μm, an accelerating voltage of 10 kV, and a beam current of 51 nA. Quantitative analysis was performed using dense TaC and HfC bulks as standard reference materials, and both standard reference materials and combinatorial material chips were loaded into the EPMA chamber for 12 h prior to analysis to stabilize the carbon contamination. The value of the nonnormalized analytical total was checked to ensure the accuracy of the analytical results. Due to the small diameter of the sample patches, micro X-ray diffractometer (XRD; D8 Discover, Bruker AXS, Germany) with a Co Kα X-ray source was utilized to obtain the phase composition of the as-prepared sample patches. The X-ray energy was 6.93 keV, and the beam size was ϕ1 mm. Mechanical properties, including the effective material modulus (E) and Oliver–Pharr hardness (H) of the sample patches, were characterized by a nano indenter (G200, Agilent Technologies, USA) in a quasistatic testing model. A diamond Berkovich nanoindenter was used to collect load–displacement data using a load control mode with a linearly increasing load to 1 gf, which was held for 10 s before the load was decreased, and the indentation depth was maintained at 10% of the coating thickness to avoid the influence of the substrate.

2.3 High-throughput oxidation of the $Ta_{1-x}Hf_xC_y$ combinatorial material chip

High-throughput oxidation was conducted in a muffle furnace (LHT 08/18/P570, Nabertherm IndustrialFurnaces Co., Ltd., Germany) with static air as the experimental atmosphere. Combinatorial material chips, which were deposited on polycrystalline Al_2O_3 substrates, were placed into a ZrO_2 crucible and then heated together in a furnace (LHT 08/18/P570, Nabertherm Industrial Furnaces Co., Ltd., Germany) to reach test temperatures, i.e., 1200, 1400, and 1600 °C, within 45 min. After annealing, combinatorial material chips were cooled to room temperature and removed. The phase composition and surface morphology of the oxidized thin film sample patches were analyzed using micro-XRD and SEM, respectively. Moreover, the cross-sectional morphology and elemental distribution of the oxidized sample patches were analyzed using a focused ion beam-scanning electron microscope (FIB-SEM; Helios 5 UX, FEI, USA).

A protective W layer was applied by focused electron beam-induced deposition to protect the area of interest (AOI) from the destructive effects of the ion beam. Then, gallium ions were used to remove the pre-AOI materials, and the penetration depth gradually increased until the substrate appeared. The cross section was ground and polished with a smaller beam current before analysis. The cross section was prepared perpendicular to the ion beam, and cross-section imaging and energy dispersive spectroscopy (EDS) analysis were also performed at this position. Furthermore, transmission electron microscopy (TEM) specimens were extracted from the oxidized sample patches via a FIB (Helios nanolab 600, FEI, USA). Subsequently, these specimens were analyzed using a TEM (Tecnai F20, FEI, USA) with the aim of verifying the crystal structures of the oxidation products.

3 Results

3.1 Characterization of combinatorial $Ta_{1-x}Hf_xC_y$ chips

To establish reliable composition-property relationships through high-throughput screening on combinatorial $Ta_{1-x}Hf_xC_y$ chips, detailed characterization among film sample patches was conducted in advance. According to the scanning profile results, the thickness of the sample patches on the combinatorial material ranges from 1.11 to 1.42 μm. Sample patches located near the elemental targets are thicker than those in the middle of the substrate, and increasing the sputtering power also promotes their thickness. All $Ta_{1-x}Hf_xC_y$ sample patches exhibit sufficient thickness to eliminate the influence from the substrate during EPMA, as the estimated X-ray generation range is approximately one hundred nanometers based on the classic Castaing formula [30]. Three combinatorial $Ta_{1-x}Hf_xC_y$ chips were obtained with compositional spans of 21.0 to 46.9 at% Ta, 13.3 to 32.9 at% Hf, 39.2 to 50.6 at% C, 13.8 to 38.8 at% Ta, 24.6 to 50.7 at% Hf, 35.5 to 44.1 at% C, 21.2 to 51.1 at% Ta, 15.7 to 40.0 at% Hf, and 33.2 to 49.1 at% C, respectively. Overlaps in the compositional range make it possible to use the sample patches for checking and verifying the material property measurement. Thereafter, as shown in Fig. 1(a), the total composition distribution among the three combinatorial material chips is summarized and plotted onto a $Ta_{1-x}Hf_xC_y$ ternary compositional map with x = 0.22 to 0.78 and y = 0.66 to 1.00, providing a broad material library containing over 100 sample patches for the downselection of chemical compositions. The roughness of the sample patches on the sapphire substrate (R_a) ranges from 6 to 10 nm. Given that this is approximately two orders of magnitude smaller than the indentation depth of hundreds of nanometers, the influence of surface roughness on the calculated contact area and unloading stiffness is negligible [31].

Moreover, carbon deficiency in transition metal carbides may induce a series of secondary phases, thereby influencing their thermal/mechanical properties [32]. Micro-XRD analysis reveals the phase evolution of thin film sample patches with varying carbon content, and six selected diffraction patterns representing the whole carbon stoichiometric span are summarized in Fig. 1(b). The sharp diffraction peaks correspond to the polycrystalline Al_2O_3 substrate, and the broadened diffraction peaks at approximately 40.9°, 47.5°, and 66.3° are assigned to the (111), (200), and (220) reflections of the face-centered cubic (FCC) structure, respectively, indicating that all $Ta_{1-x}Hf_xC_y$ sample patches maintain the same crystal structure without a secondary phase. Magnetron sputtering is a nonequilibrium process for material synthesis that promotes the formation of FCC structures in the deposition of transition metal carbide films, such as ZrC [33]. In addition, the shift in the diffraction peaks reflects the variation in the lattice parameters with the elemental composition. On the one hand, with increasing carbon content, the lattice constants of transition metal carbides, such as TaC_y, increase and approach a maximum with y of approximately 0.8, beyond which the lattice parameter decreases [34]. This contraction of the crystal structure arises from the increasing bond strength associated with higher carbon content. Meanwhile, the lattice parameters of solid solutions are modulated by the Ta/Hf ratio, as the atomic radius of Hf (0.216 nm) is larger than that of Ta (0.209 nm).

In addition to film thickness and secondary phase, the effect of composition on nanoindentation and oxidation investigation cannot be isolated in the presence of significant microstructural variations across the combinatorial material chip. The surface morphology of sample patches is inspected across the combinatorial material chips, and representative low magnification SEM images are summarized in Fig. 2, in which three typical locations covering central, half diameter, and edge on the combinatorial material chip are chosen. The corresponding high-magnification SEM morphologies (Fig. S2 in the ESM) and the analysis of the underlying formation mechanism for the as-deposited film sample patches are detailed in the ESM. In general,

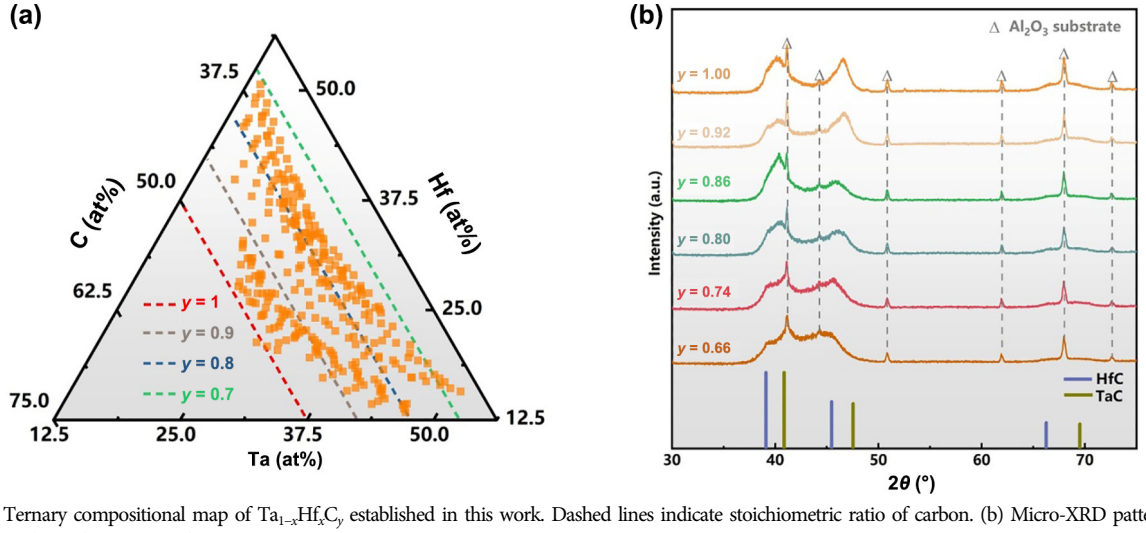

Fig. 1 (a) Ternary compositional map of $Ta_{1-x}Hf_xC_y$ established in this work. Dashed lines indicate stoichiometric ratio of carbon. (b) Micro-XRD patterns of as-prepared sample patches across carbon content span.

the film microstructures reproduce the corresponding substrate surface morphology. No visible characteristics of sample patches are observed due to the ultralow surface roughness of the sapphire substrate, ensuring the reliability of nanoindentation testing. Meanwhile, the grain size of the as-deposited sample patches is much smaller than that of the polycrystalline Al_2O_3 substrate, allowing the film microstructure to reproduce the rough substrate surface and providing a preoxidation morphology for comparison with that after oxidation. The above analyses indicate that the sample patches for mechanical property measurements show no secondary phases or visible structural differences. All sample patches deposited on the sapphire substrate are sufficiently thick and have appropriately low surface roughness for nanoindentation testing. Moreover, sample patches deposited on the Al_2O_3 substrate also exhibit comparable initial morphology. Therefore, chemical composition can be considered the primary variable in this high-throughput study.

3.2 Composition-mechanical property relationships of $Ta_{1-x}Hf_xC_y$ ceramics

As exhibited in Figs. 3(a) and 3(b), the results of the effective E and H are plotted directly onto the $Ta_{1-x}Hf_xC_y$ ternary compositional map. Meanwhile, representative nanoindentation load–displacement curves for specific $Ta_{1-x}Hf_xC_y$ sample patches are drawn in Fig. S3 in the ESM, and raw mechanical property data are provided in Table S2 in the ESM to support the reliability of the nanoindentation test. Overall, the modulus and hardness range from 202.0 to 531.0 and 20.6 to 32.1 GPa, respectively. Generally, the modulus and hardness in the present work are close to the published results from single-composition bulk samples [3,11]. Table S3 in the ESM provides a detailed comparative analysis of the absolute hardness and modulus values between the thin-film sample patches in this study and comparable bulk materials reported in recent literature. Figures 3(a) and 3(b) show that both the modulus and hardness reach their global maximum values when the composition approaches $Ta_{0.5}Hf_{0.5}C$ and then decrease gradually with decreasing C content. Furthermore, the compositional areas exhibiting maximum values are precisely distinguished. One area is around $Ta_{0.5}Hf_{0.5}C$, in which sample patches exhibit maximum values of both hardness and modulus. The evolution trend of the hardness is combined with that of the modulus to reveal the accurate Ta/Hf distribution with an optimal solid solution strengthening effect in carbon-sufficient $Ta_{1-x}Hf_xC$ carbides, which is $Ta_{0.4}Hf_{0.6}C$–$Ta_{0.45}Hf_{0.55}C$. Similar trends have been reported for $Ti_{1-x}Ta_xC$ ceramics (x = 0.1–0.9), in which the maximum hardness was obtained when x = 0.4 [35]. The other compositional area refers to a Ta-rich region (x = 0.22–0.50) with carbon vacancies (y = 0.80–1.00), where sample patches maintain a high hardness but exhibit a relatively lower modulus, which is beneficial for reducing thermal stress and promoting thermal shock resistance. Moreover, $Ta_{0.8}Hf_{0.2}C_{0.8}$, which has been reported to exhibit potential plasticity, is also located in this region. Based on the obtained mechanical property datasets, the ratio of hardness to modulus (H/E), which has been a well-accepted parameter in fracture mechanics for evaluating the damage tolerance of ceramics, was calculated as a descriptor to rapidly assess the plastic behavior potential of $Ta_{1-x}Hf_xC_y$. Typically, the H/E values of ceramics range from 0.02 to 0.1, while those possessing higher damage tolerance tend to have lower H/E values, such as yttria-stabilized zirconia (YSZ) (H/E = 0.06) and Si_3N_4 (H/E = 0.05) [36,37]. As shown in Fig. 3(c), $Ta_{1-x}Hf_xC_y$ ceramics within the aforementioned two compositional regions

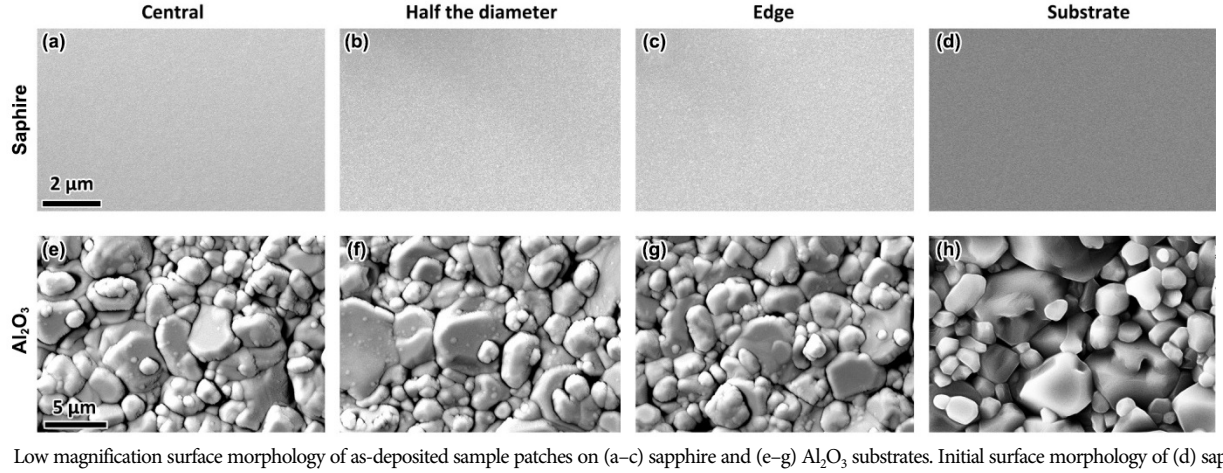

Fig. 2 Low magnification surface morphology of as-deposited sample patches on (a–c) sapphire and (e–g) Al_2O_3 substrates. Initial surface morphology of (d) sapphire and (h) Al_2O_3 substrates.

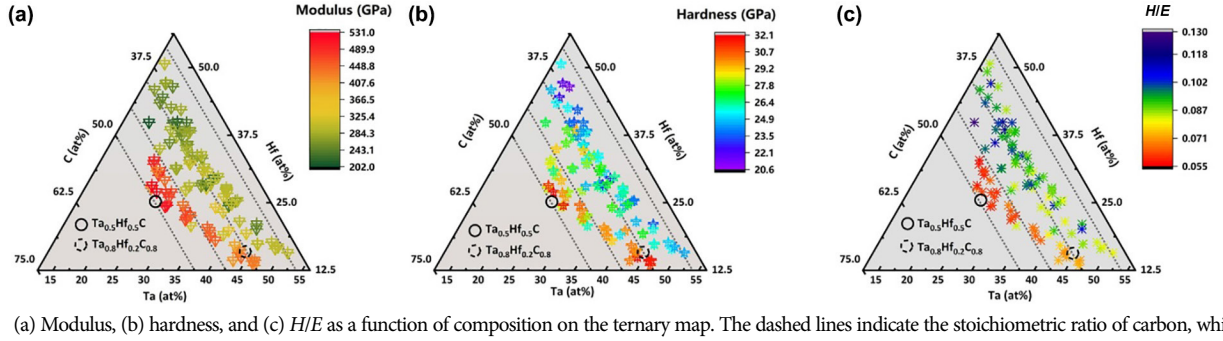

Fig. 3 (a) Modulus, (b) hardness, and (c) H/E as a function of composition on the ternary map. The dashed lines indicate the stoichiometric ratio of carbon, while the solid and dashed circles mark the locations of $Ta_{0.5}Hf_{0.5}C$ and $Ta_{0.8}Hf_{0.2}C_{0.8}$, respectively.

also display relatively lower H/E values across the compositional map due to an appropriate cooperation of hardness and modulus, indicating that they may combine damage tolerance with high strength, warranting further investigation through microfracture toughness tests or bulk sample tests. In summary, the fundamental relationships between the mechanical properties and chemical compositions of $Ta_{1-x}Hf_xC_y$ ceramics are efficiently compiled through high-throughput screening of over 100 sample patches, and the obtained property values and evolution trends are comparable to those from traditional research paradigms, providing a reliable database for designing advanced carbides.

3.3 Composition-oxidation behavior relationship of $Ta_{1-x}Hf_xC_y$ ceramics

For effective protection during oxidation or ablation, the formation of a densely packed, adherent, and rapidly sintering scale is essential, a process strongly dependent on the transition metal species. In this section, high-throughput static oxidation tests were conducted at 1200, 1400, and 1600 °C to establish a comprehensive map containing the evolution trends of the oxidation products' phase constitution, compactness, and stability with various distributions of Ta and Hf. Thus, the XRD results are correlated with varying x in $Ta_{1-x}Hf_x$ with an interval of approximately 0.05 to accurately identify the optimal stoichiometric ratio of transition metal elements and establish the preferential oxidation thermodynamics as a function of $Ta_{1-x}Hf_x$ combination.

Figure 4(a) shows XRD patterns of oxidized sample patches after exposure to 1200 °C, in which x ranges from 0.25 to 0.78. In Ta-rich sample patches (x = 0.25–0.50), Ta_2O_5 is detected as the dominant phase with traces of $Hf_6Ta_2O_{17}$. Ta_2O_5 is identified as a low-temperature orthorhombic polymorph with *Pmm*2 symmetry, and $Hf_6Ta_2O_{17}$ exhibits an orthorhombic polymorph from room temperature to the melting point. With increasing Hf content, the formation of $Hf_6Ta_2O_{17}$ is promoted, and the diffraction peak intensity of Ta_2O_5 decreases. Then, the strong diffraction peaks indicate that the oxide scale comprises nearly pure $Hf_6Ta_2O_{17}$ when x = 0.50–0.70. In addition, monolithic HfO_2 is detected in sample patches with higher Hf content, especially for $Ta_{0.25}Hf_{0.75}C$, which is expected to form single phase $Hf_6Ta_2O_{17}$. With increasing Hf content (x > 0.7), oxidation products consist of $Hf_6Ta_2O_{17}$ and HfO_2 in sample patches. Clearly, the oxidation products of $Ta_{1-x}Hf_xC_y$ ceramics indicate a further interaction between Ta_2O_5 and HfO_2, in which the increase in HfO_2 consumes Ta_2O_5 and promotes the formation of $Hf_6Ta_2O_{17}$ [20]. As shown in Fig. 4(b), the evolution of major oxide products with varying x reveals that $Hf_6Ta_2O_{17}$ is the dominant phase in the composition range of $Ta_{0.5}Hf_{0.5}$ to $Ta_{0.3}Hf_{0.7}$. Moreover, the surface morphology of the oxidized sample patches with four representative compositions across the compositional span is inserted in Fig. 4(b), in which rough and discontinuous oxidation scales containing agglomerates of refined grains are observed. The morphology of the oxide scale does not change with composition, and the discontinuity is related to the formation of gaseous oxide products as well as the low oxidation temperature, preventing sintering of solid oxide products, which has been widely observed for transition metal carbides. Sintering of oxidation products usually begins at approximately 0.6 T_m, where T_m is the melting point [38]. The melting points of Ta_2O_5, $Hf_6Ta_2O_{17}$, and HfO_2 are 1800, 2450, and 2800 °C, respectively, thereby leading to no significant sintering of the oxidation products. Therefore, the results at 1200 °C provide a basic evolution map of the phase constitution with varying compositions.

In addition to composition, the compactness of oxidation products is significant for the oxidation resistance of ultrahigh-temperature ceramics. Another $Ta_{1-x}Hf_xC_y$ combinatorial chip was oxidized at 1400 °C to promote the growth and sintering of oxidation products. Figure 5(a) depicts the phase constitution as a function of composition after oxidation. Notably, in $Ta_{1-x}Hf_x$ with x = 0.25 to 0.40, the oxidation products consist of the Ta_2O_5 dominant phase and $Hf_6Ta_2O_{17}$ secondary phase. Ta_2O_5 is identified as a monolithic structure, which is related to the phase transition of Ta_2O_5. Ta_2O_5 with a tetragonal structure (T-Ta_2O_5) is the equilibrium phase at over 1360 °C, while it cannot be maintained at room temperature and forms a metastable monolithic phase (M'-Ta_2O_5) during the cooling period [20].

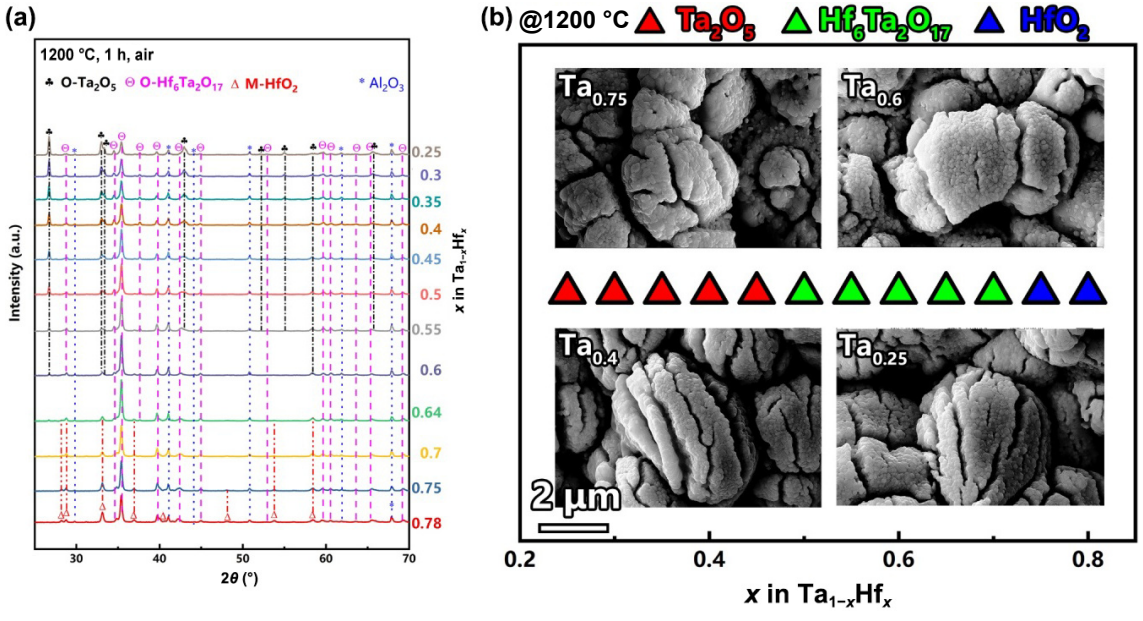

Fig. 4 (a) Micro-XRD patterns of typical sample patches after oxidation at 1200 °C. (b) Dominant phase evolution in oxidation products with x in $Ta_{1-x}Hf_x$. Inserted images show representative surface morphologies of the four sample patches. The triangle symbols represent the predominant phase in the oxidation products, as identified in (a).

With increasing Hf content, nearly pure $Hf_6Ta_2O_{17}$ is identified in the composition ranging from $Ta_{0.6}Hf_{0.4}$ to $Ta_{0.4}Hf_{0.6}$, while monolithic HfO_2 appears and gradually becomes the major phase in the oxidation products of Hf-rich sample patches. As shown in Fig. 5(b), the optimal compositional range is suggested as $Ta_{0.6}Hf_{0.4}$ to $Ta_{0.4}Hf_{0.6}$ according to the phase constitution after 1400 °C oxidation. Thereafter, typical sample patches, including $Ta_{0.6}Hf_{0.4}$, $Ta_{0.5}Hf_{0.5}$, $Ta_{0.4}Hf_{0.6}$, and $Ta_{0.3}Hf_{0.7}$, are selected for SEM characterization. The XRD results reveal that the oxide products in $Ta_{0.6}Hf_{0.4}$ to $Ta_{0.4}Hf_{0.6}$ are single $Hf_6Ta_2O_{17}$, and their oxide scale also exhibits a single morphology, in which pores or microcracks disappear, and compact oxide layers cover the rough Al_2O_3 substrate. However, the $Ta_{0.3}Hf_{0.7}$ sample patch possesses both $Hf_6Ta_2O_{17}$ and HfO_2 in the XRD pattern, and additional loose secondary oxide grains are observed on the surface. These trends in morphology indicate an accurate composition threshold to obtain a dense oxidation scale.

As 1600 °C is considered the threshold temperature for ultrahigh-temperature ceramic applications, the third set of high-throughput static oxidation experiments was conducted at 1600 °C, enabling this work to span conditions from high-temperature to ultra-high-temperature regimes. Figure 6(a) exhibits the XRD spectra of typical sample patches after oxidation. Notably, no detectable oxidation products are identified in sample patches from $Ta_{0.75}Hf_{0.25}$ to $Ta_{0.4}Hf_{0.6}$, while only HfO_2 is found in sample patches with higher Hf contents. The oxidation morphology in Fig. 6(b) confirms the XRD results, in which sparse and abundant white oxide particles are observed on $Ta_{0.6}Hf_{0.4}$ to $Ta_{0.4}Hf_{0.6}$ and $Ta_{0.3}Hf_{0.7}$ sample patches, respectively. Through EDS equipped on SEM, the white particles are confirmed as HfO_2. Considering that the phase constitution of oxidation products is obtained by micro-XRD with a small detection range, the signal of the minimal HfO_2 in $Ta_{0.75}Hf_{0.25}$ to $Ta_{0.4}Hf_{0.6}$ sample patches can be ignored compared with the alumina substrate. Remarkably, the

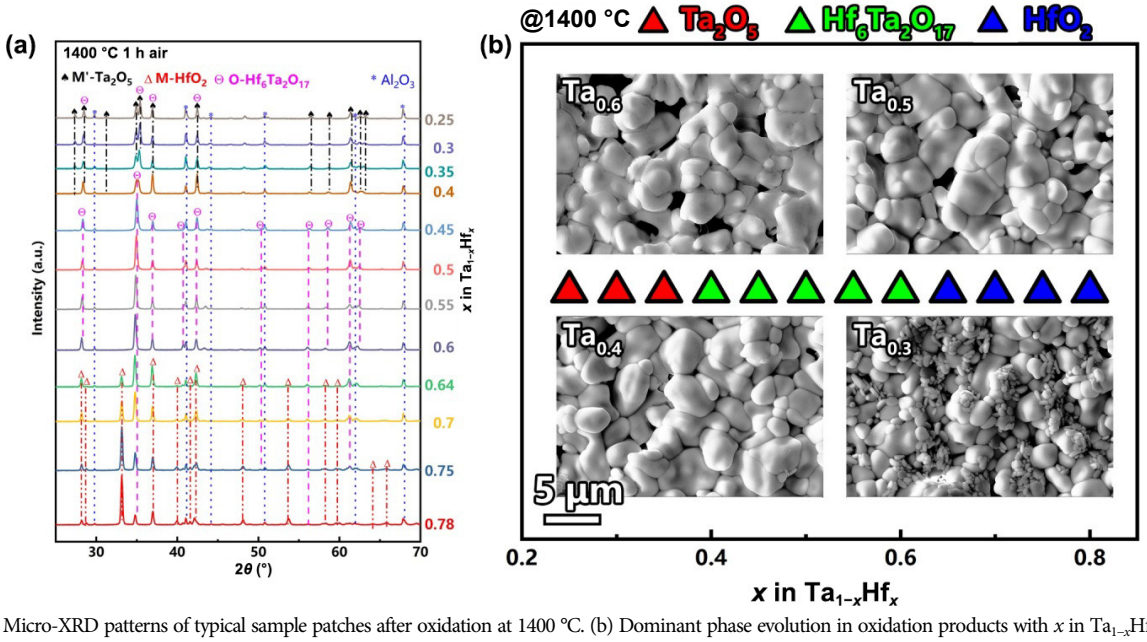

Fig. 5 (a) Micro-XRD patterns of typical sample patches after oxidation at 1400 °C. (b) Dominant phase evolution in oxidation products with x in $Ta_{1-x}Hf_x$. Inserted images show representative surface morphologies of four sample patches. Triangle symbols represent predominant phase in the oxidation products, as identified in (a).

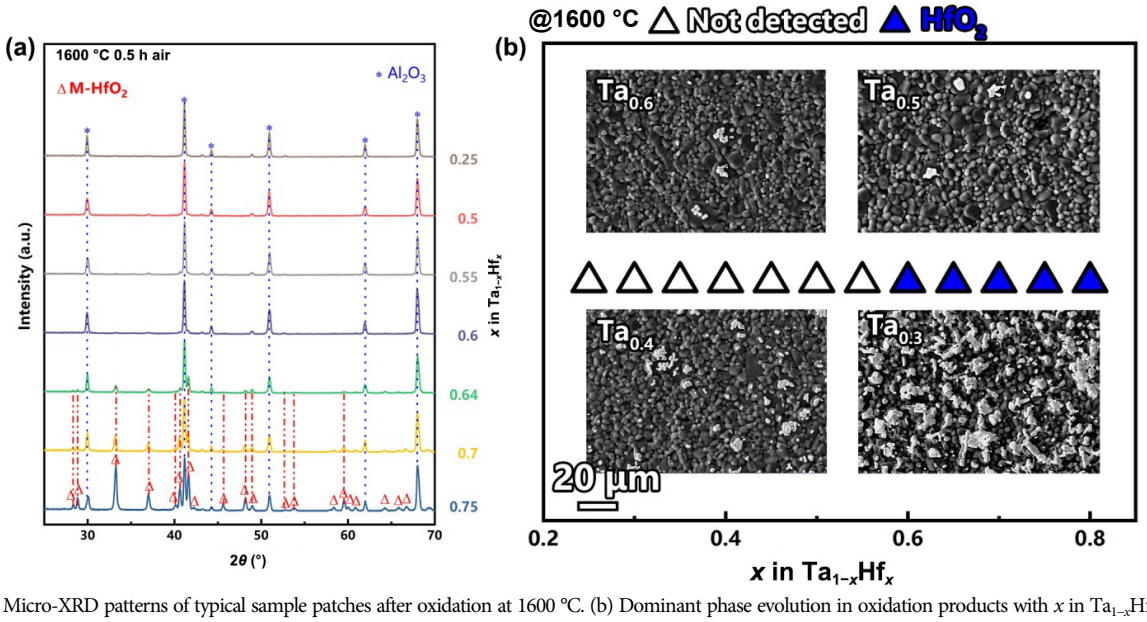

Fig. 6 (a) Micro-XRD patterns of typical sample patches after oxidation at 1600 °C. (b) Dominant phase evolution in oxidation products with x in $Ta_{1-x}Hf_x$. Inserted images show representative surface morphologies of four sample patches. Triangle symbols represent predominant phase in oxidation products, as identified in (a).

composition range (x > 0.36) for obvious HfO_2 appearing is consistent with the results at lower temperatures (1200 and 1400 °C), indicating a severe loss of tantalum during 1600 °C oxidation. Compared with bulk or coating samples, sample patches on combinatorial material chips exist in the form of thin films, which are more sensitive to gaseous oxidation products and can intuitively reflect the trend of structural stability in oxidation products with varying composition. These results emphasize that increasing the Ta content will significantly hinder the formation of dense oxide surfaces.

In addition to the phase constitution, the distribution of transition metal elements among distinct oxides provides critical insights for comprehensively understanding the composition-dependent oxidation thermodynamics in multicomponent carbides. Based on Figs. 4–6, two film sample patches, i.e., $Ta_{0.5}Hf_{0.5}$ and $Ta_{0.3}Hf_{0.7}$, were selected to track the element distribution evolution with temperature, which is detailed in Fig. S4 in the ESM. Surface EDS results indicate that Ta and Hf elements are intermixed within different oxides. Because the oxidation products after 1200 °C oxidation exhibit excessively small grain sizes and evident Ta loss along with oxide-layer degradation occurs after 1600 °C oxidation, sample patches oxidized at 1400 °C were selected for subsequent cross-sectional analysis via FIB-SEM. As shown in Fig. 7, the protective W layer, oxide layer, and Al_2O_3 substrate are marked in the cross-section images. Notably, continuous oxide layers are observed in the $Ta_{0.6}Hf_{0.4}$ to $Ta_{0.4}Hf_{0.6}$ sample patches, while loosely packed secondary grains are only observed in the $Ta_{0.3}Hf_{0.7}$ sample patch. The elemental composition of oxide grains was analyzed through EDS equipped with FIB-SEM, and the results are summarized in Table 1. The large grains in all sample patches are identified as complex Hf–Ta–O compounds, and the refined grains in the $Ta_{0.3}Hf_{0.7}$ sample patch are deduced as Ta-doped HfO_2, as obvious Hf enrichment is observed. In addition to the elemental composition, the crystal structure of these typical grains among sample patches was confirmed by TEM. A typical grain boundary between the two distinct grains in the $Ta_{0.3}Hf_{0.7}$ sample patch (area B in Fig. 7(d)) is shown in Fig. 8(a), where the high-resolution transmission electron microscopy (HRTEM) and selected area diffraction pattern (SAED) results confirm that the larger and refined grains correspond to $Hf_6Ta_2O_{17}$ and HfO_2, respectively. The EDS mapping image demonstrates a nonuniform elemental distribution: Hf is distributed in both HfO_2 and $Hf_6Ta_2O_{17}$ grains, while Ta is detected in both grains and mainly accumulates in large grains. In contrast, Fig. 8(b) reveals that the elemental distribution is uniform between the adjacent large grains (area A in Fig. 7(b)) in the $Ta_{0.5}Hf_{0.5}$ sample patch, which are identified as $Hf_6Ta_2O_{17}$. In summary, the aforementioned high-throughput results provide systematic evidence regarding phase composition and elemental distribution features, which lays a solid foundation for the subsequent discussion on the oxidation mechanism.

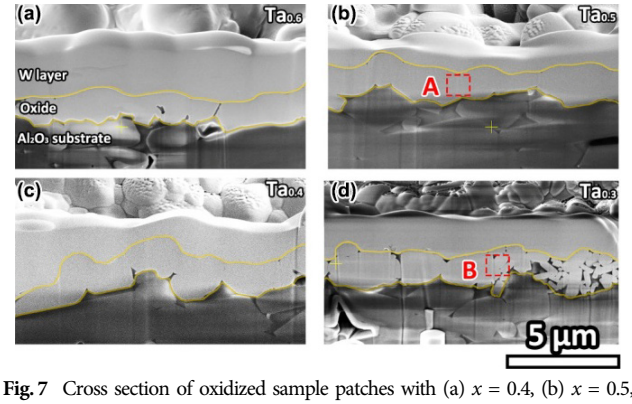

Fig. 7 Cross section of oxidized sample patches with (a) x = 0.4, (b) x = 0.5, (c) x = 0.6, and (d) x = 0.7 in $Ta_{1-x}Hf_xC_y$. Oxide layer is highlighted between protective W layer and substrate. Areas marked with boxes, labeled A and B, show typical grain boundaries for TEM characterization.

4 Discussion

4.1 Composition design for optimal mechanical properties

Previous studies have shown that in the stoichiometric $Ta_{1-x}Hf_xC$ system, the hardness and modulus generally approach their maximum values at approximately x = 0.5. The results of high-throughput screening further refine and specify the trend of properties with composition. This refinement is possible due to the nearly continuous variation in composition and the fact that all thin-film sample patches share a similar, single-phase microstructure. As shown in Fig. 9(a), the evolution trends in hardness and modulus reveal that the hardest carbon sufficient $Ta_{1-x}Hf_xC$ is $Ta_{0.4}Hf_{0.6}C$ to $Ta_{0.45}Hf_{0.55}C$. These composition-dependent trends are attributed to the synergistic effects of solid solution strengthening and electronic structure evolution with various Ta/Hf ratios. The substitution of Hf for Ta (or *vice versa*) introduces a significant atomic size mismatch, leading to pronounced lattice distortion. The degree of this strengthening is maximized at intermediate compositions where the mutual strain effects are most severe. Moreover, for rock-salt structure transition metal carbides or nitrides with strong covalent bonding characteristics, the valence electron concentration (VEC) has been considered a significant indicator of mechanical properties. Figure 9(b) exhibits the VEC as a function of x with y = 1.0 to 0.7. The VEC of $Ta_{0.5}Hf_{0.5}C$ is 8.5 per cell, and it slightly decreases to 8.4 in $Ta_{0.4}Hf_{0.6}C$, which approaches the theoretically optimal range (8 to 8.4 per formula unit) to obtain the strongest covalent bonding and highest elastic constants, contributing to high hardness and modulus [39,40]. Similar trends have been reported in recent theoretical simulations as well as experimental studies [11,41], governing the reliability of high-throughput screening.

In addition to the Ta/Hf ratio, the carbon vacancy provides a broad range for composition regulation. As shown in Fig. 9(b), after introducing minimal carbon vacancies (y = 0.90), the VEC of

Table 1 Elemental composition of different grains within oxidation layer in Fig. 7

Position	Sample patche	Composition		
		Ta (at%)	Hf (at%)	O (at%)
Large grain	$Ta_{0.6}Hf_{0.4}$	15.6±0.5	14.8±0.8	69.6±0.4
	$Ta_{0.5}Hf_{0.5}$	15.0±1.1	19.4±1.0	65.6±1.8
	$Ta_{0.4}Hf_{0.6}$	10.1±0.2	19.8±0.5	70.1±0.6
	$Ta_{0.3}Hf_{0.7}$	9.7±0.1	22.3±0.3	68.0±0.3
Refined grain	$Ta_{0.3}Hf_{0.7}$	3.7±0.2	32.1±2.4	64.2±2.6

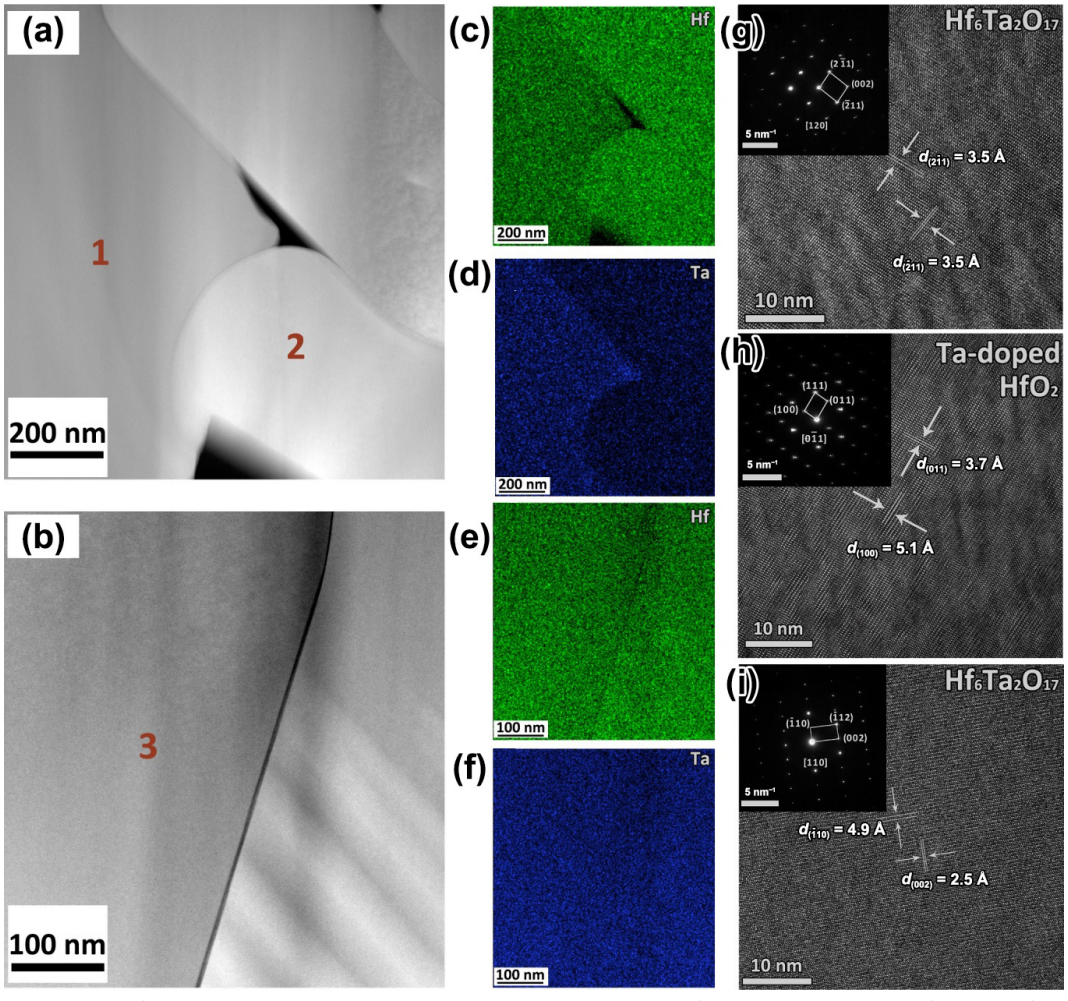

Fig. 8 High-angle annular dark-field imaging (HAADF) images and corresponding element mapping of oxide layer in (a, c, d) $Ta_{0.3}Hf_{0.7}$ and (b, e, f) $Ta_{0.5}Hf_{0.5}$. HRTEM inserted with SAED images of grains (g) 1, (h) 2, and (i) 3.

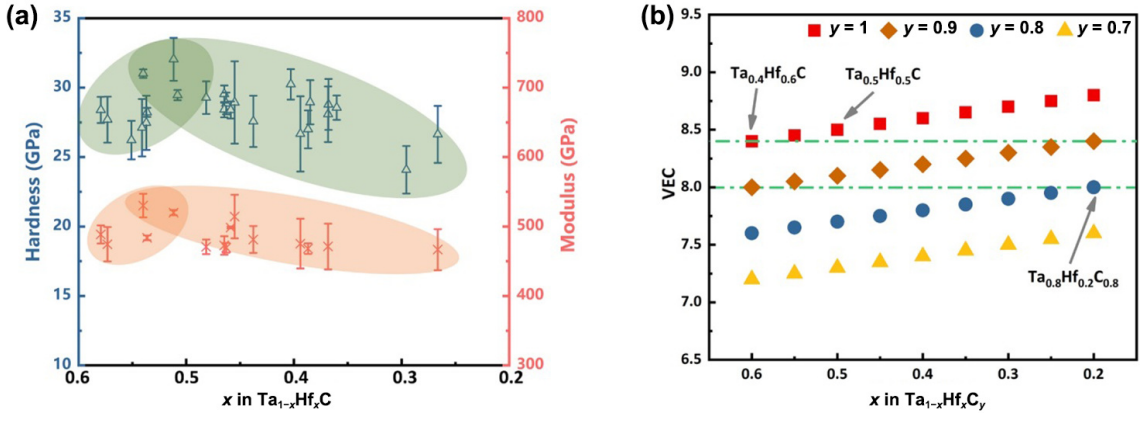

Fig. 9 (a) Evolution of hardness and modulus as a function of x in $Ta_{1-x}Hf_xC_y$ with y = 1. (b) Variation of VEC in $Ta_{1-x}Hf_xC_y$ with x and y. Dashed lines represent optimal VEC value (8 to 8.4 per unit).

$Ta_{1-x}Hf_xC_y$ sample patches are still located in the optimal region, assuring high hardness (25 to 32 GPa) and modulus (450 to 530 GPa) comparable to the stoicmetric counterparts. Moreover, the colored map in Fig. 3(a) reveals different decreasing trends between Hf-rich sample patches and Ta-rich patches with increasing C vacancies. As the C content decreases to approximately 45 at% (y = 0.80), the moduli of Hf-rich (x = 0.60 to 0.70) sample patches are below 300 GPa, while Ta-rich sample patches (x = 0.20 to 0.50) maintain moduli of approximately 400 GPa with similar carbon vacancies, indicating that excess Ta^{5+} metallic cations in Ta-rich sample patches provide extra valence electrons to alleviate the elastic modulus decrease at low carbon vacancy concentrations [42]. Different from the modulus, which is strongly determined by bonding characteristics and follows trends similar to those of the lattice elastic constant, the hardness is influenced by multiple mechanisms, including dislocation motion, lattice distortion, and point defects. Since the decrease in the bonding strength of Ta-rich samples is moderate, Hf atoms and

carbon vacancies provide additional hardening effects, including lattice distortion and pinning of dislocations; thus, Ta-rich sample patches with $y = 0.80$ to 1.00 exhibit a second maximum hardness, which is experimentally observed in the group VB transition metal carbides [43]. With y further decreasing in $Ta_{1-x}Hf_xC_y$, increasing carbon depletion leads to gradual delocalization from strong covalent bonding of carbon–metal to metallic–character bonding, contributing to a decrease in the elastic constant, and all sample patches exhibit a modulus below 300 GPa when $y < 0.80$ [44,45]. Based on the above results, the threshold value of y is restricted to 0.80, below which the softer characteristics are dominant. In summary, compared with the whole composition region ($x = 0.22$ to 0.78, $y = 0.66$ to 1.00), the composition of $Ta_{1-x}Hf_xC_y$ could be tuned from $x = 0.22$ to 0.60 and $y = 0.80$ to 1.00 to design carbides possessing relatively lower modulus, which is beneficial for thermal shock resistance, lower H/E value, indicating promising damage tolerance, and high hardness to withstand mechanical erosion.

4.2 Compositional design for optimal oxidation resistance

The Gibbs free energies of the oxidation reaction (ΔG°) of TaC and HfC were calculated, as oxidation thermodynamics provide the foundation for understanding oxidation mechanisms. As shown in Fig. 10(a), the oxidation of HfC is favored over TaC in the present experimental conditions (at 1200–1600 °C in an atmospheric environment). Compared with group ⅤB metallic elements (Ta, Nb), group ⅣB metallic elements (Ti, Zr, and Hf) preferentially form oxides due to their lower oxidation reaction free energies, and this oxidation sequence is also suitable for multicomponent systems under different oxidation conditions [23,24] and carbon vacancies [15]. Considering that the initial carbides are in the solid solution state, HfO_2 doped with a minimal amount of Ta during the initial oxidation of $Ta_{1-x}Hf_xC_y$ ceramics, which is also confirmed by the surface and cross-section EDS results. Thereafter, the preferential formation of Hf oxide depleted the Hf content in $Ta_{1-x}Hf_xC_y$ ceramics, and then the concentration of Ta increased to a sufficient value to promote the formation of Ta_2O_5. This is also confirmed by Figs. 4 and 5, in which detectable Ta_2O_5 is observed at high Ta content. Finally, Ta_2O_5 reacted with abundant HfO_2 to form $Hf_6Ta_2O_{17}$. Due to the initial Ta consumption during the formation of Ta-doped HfO_2, the optimal value for the Ta/Hf distribution shifts to a Ta-rich region to provide additional Ta, ensuring the formation of single-phase $Hf_6Ta_2O_{17}$. In addition, $Ta_{0.5}Hf_{0.5}C$, which exhibits the best oxidation resistance in the distributed single-composition investigation, falls within the optimal compositional range. It should be noted that although the complex Hf–Ta–O compound grains are identified as $Hf_6Ta_2O_{17}$, the Hf/Ta ratios in these compounds among all sample patches are obviously below the ideal value (Hf/Ta = 3) calculated from this chemical formula. On the one hand, the crystal structure of $Hf_6Ta_2O_{17}$ could intrinsically accommodate the deviation in the Hf/Ta ratio by removing sets of symmetry-equivalent seven-coordinated polyhedral structural units in the sublattice, leading to homologous compounds, such as $Hf_4Ta_2O_{13}$ (Hf/Ta = 2) [46]. On the other hand, it has been reported that the actual distribution of Hf and Ta atoms is disordered in these structures, as these cations share similar cation-oxygen bond lengths in the crystal structure [47]. The present

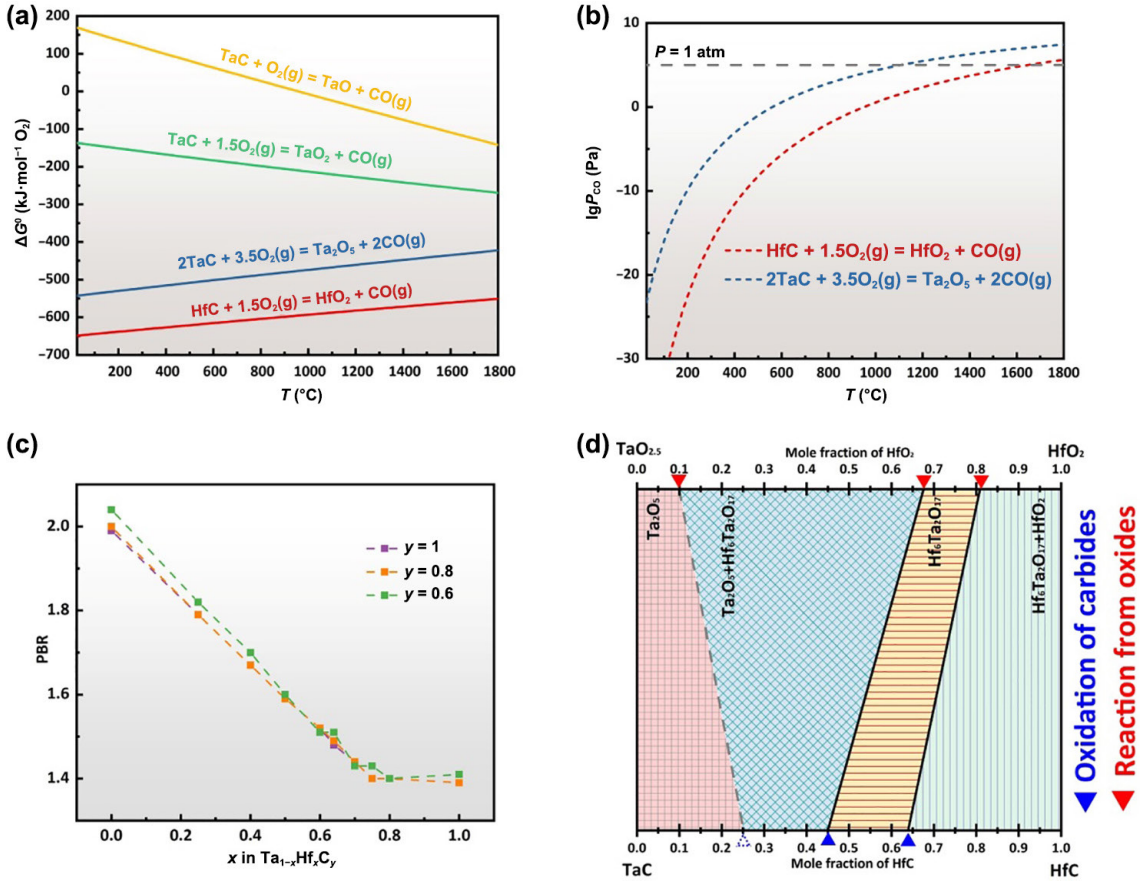

Fig. 10 (a) Evolutions of reaction free energies per mol O_2 with temperature of typical oxides in $Ta_{1-x}Hf_xC$ ceramics. (b) Evolutions of vapor pressure of CO at TaC/Ta_2O_5 interface and HfC/HfO_2 interface with temperature, respectively. (c) Evolution of P_{BR} with composition. (d) Composition balance diagram linking Hf–Ta–O oxides and Hf–Ta–C carbides binary systems based on high-throughput oxidation investigations.

Hf–Ta–O compounds are generated from Ta-doped HfO_2 and Ta_2O_5; thus, the Hf/Ta ratio was further reduced compared with the theoretical value range (Hf/Ta ratio = 2 to 3).

Moreover, severe Ta loss and instability of oxide layers occurred on Ta-rich ($x < 0.36$) sample patches after oxidation at 1600 °C, which requires further analysis. One potential mechanism is the formation of gaseous Ta oxides, such as TaO and TaO_2. As shown in Fig. 10(a), the results confirm that HfO_2 and Ta_2O_5 are thermodynamically stable, whereas gaseous Ta oxides are not favored at 1600 °C under ambient conditions, indicating that Ta did not vaporize in the form of gas. As bulk samples of a similar composition ($Ta_{0.8}Hf_{0.2}C$) under the same conditions (1600 °C in air) did not show severe Ta loss [22], the observed difference is likely attributable to the sample form. On the one hand, the pressure of gaseous carbon oxides, such as CO, increases rapidly with temperature. The evolution of CO vapor pressure at the carbide/oxide interface with temperature was also calculated using thermodynamic data from thermodynamic calculation software HSC Chemistry 6.0 (Outokumpu Technology, Finland) based on the methodology described in the ESM and presented in Fig. 10(b). The vapor pressure of CO at the TaC/Ta_2O_5 interface increases more rapidly than that at the HfC/HfO_2 interface with increasing temperature and significantly exceeds 1×10^5 Pa at 1600 °C. On the combinatorial material chip, oxidation rapidly propagated through the entire thin film sample patches due to their limited thickness of 1 to 2 μm. For Ta-rich sample patches, thin films were directly broken or burst by high vapor pressure CO, leading to no detectable oxidation products. Meanwhile, HfO_2 formed and sintered preferentially at the oxide scale of Hf-rich sample patches, and then the Hf-consumed sample patches formed Ta_2O_5, which was broken by accompanying high-pressure CO, leaving discontinuous oxide scales on the combinatorial chip. Another mechanism involves the volume change during the conversion from carbides to oxides, which is evaluated by the Pilling-Bedworth ratio (P_{BR}) [17]. Typically, a high P_{BR} indicates significant internal stress during high-temperature oxidation and hinders the formation of continuous oxide layers. The evolution of P_{BR} with composition for $Ta_{1-x}Hf_xC_y$ is estimated and presented in Fig. 10(c), and the detailed calculation procedure is described in the ESM. The P_{BR} decreases with increasing Hf content and shows little dependence on carbon content. It approaches a lower value (1.4) when $x >$ 0.36, consistent with the oxidation results where visible oxide products were obtained after 1600 °C oxidation. As the thickness increases to hundreds of micrometers in actual UHTC coatings or thousands of micrometers in structural components, the detrimental effects of CO or CO_2 vapor pressure and internal stress are reduced and are usually considered a minor factor in the formation of a porous oxide layer [38]. This finding indicates that a comprehensive analysis is needed, considering chemical composition, phase constitution, structure, and thermodynamics, to evaluate the relationship and differences in oxidation behavior between thin film sample patches and real bulk or coating samples. By comparing experimental datasets and integrating simulation calculations, the reliability of thin film experiments can be assessed, enabling rapid narrowing of the candidate material range. Subsequently, their practical application potential should be systematically validated through conventional research, establishing a connection between high-throughput screening and real applications.

Finally, an experimental composition balance diagram between the Ta–Hf–C carbide system and Ta–Hf–O oxide system is constructed based on the high-throughput oxidation results to correlate the equilibrium phase distributions of the multiphase oxides with the oxidation behavior of multicomponent carbides. As shown in Fig. 10(d), the upper x-axis follows the experimental Ta_2O_5–HfO_2 diagram from Ref. [20], in which typical compositional thresholds for phase constitution transition are marked by red triangles. The corresponding compositional boundaries derived from the current results are indicated by blue triangles on the lower x-axis. With increasing Hf content, the first boundary between Ta_2O_5 and Ta_2O_5–$Hf_6Ta_2O_{17}$ is represented by a dashed line since pure Ta_2O_5 was not detected among all sample patches after oxidation. Furthermore, the following two phase-domain boundaries (Ta_2O_5–$Hf_6Ta_2O_{17}$/$Hf_6Ta_2O_{17}$, $Hf_6Ta_2O_{17}$/$Hf_6Ta_2O_{17}$–HfO_2) lean toward the Hf-poor (Ta-rich) region due to the thermodynamic and structural characteristics discussed earlier. Considering the melting points of different oxides ($Hf_6Ta_2O_{17}$: ~2450 °C, HfO_2: ~2900 °C), this work provides an important reference for the precise design of oxide scales by tailoring the composition of carbides. Considering the similarity in oxidation tendencies among homologous transition metallic elements, this experimental equilibrium diagram facilitates an in-depth understanding of the oxidation behavior of multicomponent carbides incorporating thermodynamic principles and complex oxide formation.

5 Conclusions

In the present work, a thorough high-throughput exploration of $Ta_{1-x}Hf_xC_y$ ceramics is conducted with an emphasis on the optimization of mechanical properties and oxidation resistance for ultrahigh-temperature applications. Over 100 $Ta_{1-x}Hf_xC_y$ sample patches with precisely controlled compositional gradients (x = 0.22 to 0.78, y = 0.66 to 1.00) have been deposited in a combinatorial cosputtering system, and all sample patches possess sufficient thickness, the same FCC structure, and similar morphology, enabling reliable high-throughput exploration. Evolution trends in hardness and modulus clearly reveal that the composition of $Ta_{1-x}Hf_xC_y$ could be tuned within x = 0.22 to 0.6 and y = 0.80 to 1.00 to reach an optimal balance between hardness and toughness, enhancing the thermal shock resistance. This is achieved through the simultaneous regulation of three factors: the bonding strength (reflected by the VEC and maintained at an optimal range of 8–8.4 per formula unit), the solid solution effect (governed by the Ta/Hf ratio), and the bonding characteristics (whether covalent or metallic, which are dominated by carbon vacancies). The distribution of transition metal elements is further refined to x = 0.50 to 0.60 to form a single-phase, dense, and compact Hf–Ta–O compound layer, which is promising for enhancing the oxidation resistance of the *in situ* oxidation scale during application. Compared with previous results, the shift of this optimal compositional range to the Ta-rich region results from preferential formation of Ta-doped HfO_2 and the structural characteristics of Hf–Ta–O compounds, which accommodate composition deviation. CHT experimentation serves as a bridge between theoretical research and conventional research paradigms. It provides extensive datasets to validate the established theory for mechanical property prediction, while for oxidation behavior, the present work reveals composition-dependent preferential oxidation thermodynamics, considering the formation of complex oxidation products. The reliability of the high-throughput method is confirmed by the consistent trends between the present work and the single-composition specimen investigation. More importantly, the high efficiency is demonstrated by comprehensively revealing the composition-

property complexities in $Ta_{1-x}Hf_xC_y$ ceramics before producing bulk-like and defect-free specimens. Among the ternary compositional maps, the final $Ta_{1-x}Hf_xC_y$ composition (x = 0.50–0.60, y = 0.80–1.00) proves to be an excellent system for future oxidation studies and further applications.

Acknowledgements

This work was supported by the National Natural Science Foundation of China (Nos. U2441266, U21A2063, 52372071, and 52302076).

Author contributions

Xirui Lv: Conceptualization, Data curation, Formal analysis, Investigation, Methodology, Validation, Visualization, Writing—original draft; Yiming Lei: Formal analysis, Investigation; Jinyu Shi: Investigation; Jie Zhang: Conceptualization, Funding acquisition, Supervision, Writing—review & editing; Jingyang Wang: Supervision.

Availability of data and materials

The data that support the findings of this study are available from the corresponding author upon reasonable request.

Competing interests

The authors have no competing interests to declare that are relevant to the content of this article. The authors Jie Zhang and Jingyang Wang are the Editorial Committee members of this journal.

Electronic Supplementary Material

Supplementary material is available in the online version of this article at https://doi.org/10.26599/JAC.2026.9221252.

References

[1] Peters AB, Zhang DJ, Chen S, *et al.* Materials design for hypersonics. *Nat Commun* 2024, **15**: 3328.

[2] Savvatimskiy AI, Onufriev SV, Muboyadzhyan SA. Thermophysical properties of the most refractory carbide $Ta_{0.8}Hf_{0.2}C$ under high temperatures (2000–5000 K). *J Eur Ceram Soc* 2019, **39**: 907–914.

[3] Zhang J, Wang S, Li W. Consolidation and characterization of highly dense single-phase Ta–Hf–C solid solution ceramics. *J Am Ceram Soc* 2019, **102**: 58–62.

[4] Feng GH, Li HJ, Yang L, *et al.* Investigation on the ablation performance and mechanism of HfC coating modified with TaC. *Corros Sci* 2020, **170**: 108649.

[5] Wyatt BC, Nemani SK, Hilmas GE, *et al.* Ultra-high temperature ceramics for extreme environments. *Nat Rev Mater* 2024, **9**: 773–789.

[6] Glass D. Physical challenges and limitations confronting the use of UHTCs on hypersonic vehicles. In proceeding of the 17th AIAA International Space Planes and Hypersonic Systems and Technologies Conference, San Francisco, California, 2011: AIAA2011–2304.

[7] Zhang BH, Yin J, Huang YH, *et al.* Harmonized toughening and strengthening in pressurelessly reactive-sintered $Ta_{0.8}Hf_{0.2}C$–SiC composite. *J Eur Ceram Soc* 2018, **38**: 5610–5614.

[8] Tan ZY, Xu GN, Peng YB, *et al.* The high-toughness mechanism of heterogeneous solid solution HfC–TaC–HfO_2 composite ceramics. *Coll Compos Commun* 2024, **51**: 102097.

[9] Ren JC, Zhang YL, Zhang PF, *et al.* Ablation resistance of HfC coating reinforced by HfC nanowires in cyclic ablation environment. *J Eur Ceram Soc* 2017, **37**: 2759–2768.

[10] Chen H, Zhang YL, Fu YQ, *et al.* Novel $Hf_xTa_{1-x}C$ solid solution nanowire toughened HfC coating: An effective strategy for synchronous enhanced mechanical and anti-ablation performance. *J Adv Ceram* 2024, **13**: 590–601.

[11] Smith CJ, Yu XX, Guo QY, *et al.* Phase, hardness, and deformation slip behavior in mixed $Hf_xTa_{1-x}C$. *Acta Mater* 2018, **145**: 142–153.

[12] Zhang BH, Wang YW, Yin J, *et al.* Carbon deficiency introduced plasticity of rock-salt-structured transition metal carbides. *J Mater Sci Technol* 2023, **164**: 205–214.

[13] Hossain MD, Borman T, Kumar A, *et al.* Carbon stoichiometry and mechanical properties of high entropy carbides. *Acta Mater* 2021, **215**: 117051.

[14] Zeng Y, Wang DN, Xiong X, *et al.* Ablation-resistant carbide $Zr_{0.8}Ti_{0.2}C_{0.74}B_{0.26}$ for oxidizing environments up to 3000 °C. *Nat Commun* 2017, **8**: 15836.

[15] Lun HL, Zeng Y, Xiong X, *et al.* Oxidation behavior of non-stoichiometric $(Zr,Hf,Ti)C_x$ carbide solid solution powders in air. *J Adv Ceram* 2021, **10**: 741–757.

[16] Fang C, Dong S, Zhang XH, *et al.* Breaking the 3000 °C melting temperature barrier of oxide ceramics. *J Adv Ceram* 2025, **14**: 9221193.

[17] Li YL, He L, Pan H, *et al.* Compositional optimization for enhanced oxidation resistance of high-entropy carbide ceramics. *Acta Mater* 2025, **282**: 120463.

[18] Guo LX, Huang SW, Li W, *et al.* Theoretical design and experimental verification of high-entropy carbide ablative resistant coating. *Adv Powder Mater* 2024, **3**: 100213.

[19] Feng GH, Li HJ, Yao XY, *et al.* Effect of tantalum carbide on the ablation behaviors of hafnium carbide coating for C/C composites under single and cyclic oxyacetylene torch environments. *Surf Coat Tech* 2020, **400**: 126219.

[20] McCormack SJ, Tseng KP, Weber RJK, *et al. In-situ* determination of the HfO_2–Ta_2O_5-temperature phase diagram up to 3000 °C. *J Am Ceram Soc* 2019, **102**: 4848–4861.

[21] Zaman R, Opila EJ, Zhou BC. Thermodynamic modeling of the Hf–Ta–O system for the design of oxidation resistant HfC–TaC ceramics. *Open Ceram* 2024, **19**: 100618.

[22] Zhang J, Wang S, Li W, *et al.* Understanding the oxidation behavior of Ta–Hf–C ternary ceramics at high temperature. *Corros Sci* 2020, **164**: 108348.

[23] Backman L, Gild J, Luo J, *et al.* Part II: Experimental verification of computationally predicted preferential oxidation of refractory high entropy ultra-high temperature ceramics. *Acta Mater* 2020, **197**: 81–90.

[24] Backman L, Gild J, Luo J, *et al.* Part I: Theoretical predictions of preferential oxidation in refractory high entropy materials. *Acta Mater* 2020, **197**: 20–27.

[25] Miracle DB, Li M, Zhang ZH, *et al.* Emerging capabilities for the high-throughput characterization of structural materials. *Annu Rev Mater Res* 2021, **51**: 131–164.

[26] Lv XR, Lei YM, Zhang Z, *et al.* Accelerating the design of multicomponent rare earth silicates for SiC_f/SiC CMC by combinatorial material chip design and high throughput screening. *J Mater Sci Technol* 2023, **150**: 96–103.

[27] Li XX, Fu QG, Wen ZH, *et al.* Research progress on ultra-high temperature ceramic structural materials for extreme environments. *J Inorg Mater* 2025, **40**: 1045.

[28] Backman L, Hunter BM, Weaver ML, *et al.* Invited Article: The oxidation kinetics and mechanisms observed during ultra-high temperature oxidation of (HfZrTiTaNb)C and (HfZrTiTaNb)B_2. *J Appl Phys* 2024, **136**: 055106.

[29] Lv JS, Li W, Li T, *et al.* Multicomponent (Hf–Zr–Ta)B_2 coatings for carbon/carbon composites and structural optimization enabling superior ablation resistance. *J Mater Sci Technol* 2025, **204**: 115–126.

[30] Llovet X, Moy A, Pinard PT, *et al.* Electron probe microanalysis: A review of recent developments and applications in materials science and engineering. *Prog Mater Sci* 2021, **116**: 100673.

[31] Kim JY, Kang SK, Lee JJ, *et al.* Influence of surface-roughness on indentation size effect. *Acta Mater* 2007, **55**: 3555–3562.

[32] Zhang YH, Liu B, Wang JM, *et al.* Theoretical investigations of the

effects of ordered carbon vacancies in ZrC_{1-x} on phase stability and thermo-mechanical properties. *Acta Mater* 2016, **111**: 232–241.
[33] Chen LN, Lei YM, Zhang J, *et al.* Synthesis and characterization of ZrC_x coatings with different stoichiometry. *Vacuum* 2022, **202**: 111211.
[34] Riedl H, Glechner T, Wojcik T, *et al.* Influence of carbon deficiency on phase formation and thermal stability of super-hard TaC_y thin films. *Scripta Mater* 2018, **149**: 150–154.
[35] Xu WZ, Geng X, Xie Q, *et al.* Tunable mechanical properties and excellent microwave transparent performance of full spectrum $(Ti_xTa_{1-x})C$ microcuboids ($0 < x < 1$) synthesized via a dissolution-precipitation strategy. *Mater Charact* 2023, **201**: 112964.
[36] El-Raghy T, Zavaliangos A, Barsoum MW, *et al.* Damage mechanisms around hardness indentations in Ti_3SiC_2. *J Am Ceram Soc* 1997, **80**: 513–516.
[37] McColm IJ. *Ceramic Hardness*. Boston, MA: Springer US, 1990.
[38] Zhang C, Loganathan A, Boesl B, *et al.* Thermal analysis of tantalum carbide–hafnium carbide solid solutions from room temperature to 1400 °C. *Coatings* 2017, **7**: 111.
[39] Balasubramanian K, Khare SV, Gall D. Valence electron concentration as an indicator for mechanical properties in rocksalt structure nitrides, carbides and carbonitrides. *Acta Mater* 2018, **152**: 175–185.
[40] Jhi SH, Ihm J, Louie SG, *et al.* Electronic mechanism of hardness enhancement in transition-metal carbonitrides. *Nature* 1999, **399**: 132–134.
[41] Zhang YT, Li SM, Li N, *et al.* Experimental and theoretical study on electronic structure and mechanical property of $Ta_xHf_{1-x}C$. *J Alloys Compd* 2021, **884**: 161040.
[42] Gusev AI. Effect of defectiveness of carbon sublattice on elastic properties and microstrains of disordered cubic tantalum carbide TaC_y. *Int J Refract Met H* 2022, **103**: 105760.
[43] Chen W, Dong WW, Ma SL, *et al.* Carbon vacancy induced metallicity and lattice distortion for superior mechanical properties in niobium carbide. *J Alloys Compd* 2025, **1029**: 180796.
[44] Jhi SH, Louie SG, Cohen ML, *et al.* Vacancy hardening and softening in transition metal carbides and nitrides. *Phys Rev Lett* 2001, **86**: 3348–3351.
[45] Peng JH, Tikhonov E. Vacancy on structures, mechanical and electronic properties of ternary Hf–Ta–C system: A first-principles study. *J Inorg Mater* 2022, **37**: 51.
[46] McCormack SJ, Kriven WM. Crystal structure solution for the $A_6B_2O_{17}$ (A = Zr, Hf; B = Nb, Ta) superstructure. *Acta Crystallogr B* 2019, **75**: 227–234.
[47] Voskanyan AA, Lilova K, McCormack SJ, *et al.* A new class of entropy stabilized oxides: Commensurately modulated $A_6B_2O_{17}$ (A = Zr, Hf; B = Nb, Ta) structures. *Scripta Mater* 2021, **204**: 114139.